Radiation Heat Transfer and Reaction Chemistry Models for Risk Assessment Compatible Fire Simulations

MILES GREINER*

Department of Mechanical Engineering
University of Nevada, Reno, NV 89557, USA

AHTI SUO-ANTTILA

Alion Science and Technology Corporation, Albuquerque
NM 87110, USA

ABSTRACT: Risk assessment studies for hazardous material packages require fire response prediction tools that are both accurate and rapid. This article describes the theoretically based, semiempirical reaction chemistry and radiation heat transfer models for large, optically dense pool fires incorporated in the ISIS-3D CFD software. The chemistry model employs four separate reactions (two produce radiating soot). The heat transfer model divides the computational domain into the diffusely radiative fire and its nonparticipating environment. ISIS-3D simulations are performed on a 6-m square JP8 pool fire experiment in which the soot temperature and volume fraction are measured. The reaction rate and soot formation parameters of the chemistry model are determined based on a comparison of the simulation with the measured data. Simulations are then performed on an experiment that measures the temperature of a pipe calorimeter suspended over the leeside of a 19-m-diameter JP8 fuel pool fire with a 9.5 m/s crosswind. The soot volume fraction that the heat transfer model uses to define the edge of the diffusely radiating fire is determined based on a comparison with the measured average temperature of the calorimeter. That simulation accurately predicts the calorimeter spatial temperature variation without further adjustment. ISIS-3D is not fully predictive, should not be used far outside the range of conditions in which its parameters are determined (JP8 pool fires larger than 2 m), and is not intended to replace the fundamental fire physics software. However, it demonstrates highly accurate results with rapid turnaround times for a range of conditions that are relevant to large hazardous material transport packages in severe fire conditions.

KEY WORDS: risk assessment, radiation heat transfer, combustion chemistry, pool fire, fire simulation.

*Author to whom correspondence should be addressed. E-mail: greiner@unr.edu

1042-3915/06/02 0079–25 $10.00/0 DOI: 10.1177/1042391506054299

INTRODUCTION

HIGH-LEVEL NUCLEAR WASTE, military materials, and other hazardous substances are typically stored and transported in massive, thick wall packages. Risk assessment studies estimate the probability of accidental or intentional insults and their likely consequences [1]. These studies rely on computer tools to estimate the physical response of packages to large pool fires for a variety of wind conditions and package placements relative to the fuel source. Since multiple simulations are performed, risk assessment fire models must be rapid as well as accurate. Fortunately, they do not need to cover an extremely wide range of fire sizes because only very large fires are capable of challenging the integrity of massive packages.

Specialized fire physics software such as Kameleon from SINTEF and Vulcan from Sandia, as well as commercial computational fluid dynamics (CFD) software, such as CFX and Fluent, are capable of calculating the velocity, temperature, and species fields within a wide variety of fires. They employ highly advanced models for calculating general fire behavior from first principles but may require massive amounts of run time on specialized computing platforms. These simulations are capable of calculating conjugate conduction and radiation within objects engulfed in fires. However, they employ the same grid structure for both the flowing and solid regions. If the solid regions involve small-scale structures that require small mesh dimensions, the computational time step becomes prohibitively small. These software models are therefore not well suited for the multiple simulations of transient package response required in risk studies.

Simple fire models that involve a specified fire temperature and effective fire emissivity have also been employed [2]. They are easily linked to finite element models of the hazardous material package, and the linked model produces results with relatively short computational turnaround times. However, these models do not include the effect that wind or the object itself has on the fire.

Correlation-based risk assessment fire models provide heat flux within pool fires [3]. They are based on data from measurements and calculation of different pool sizes, fuel types, and wind conditions. However, they do not include the feedback effects that objects or enclosures may have on the fire. Furthermore, correlation-based models do not account for conditions outside the range of the correlations, for example multiple fires, odd shapes, and transient conditions.

The ISIS-3D CFD/radiation heat transfer computer software is an emerging tool for fire risk assessment studies. Its primary purpose is to predict the heat transfer distribution from large fires to massive objects with ‘engineering level’ accuracy for a variety of wind conditions and package

placements, while using reasonably short computer turnaround times. It is a general purpose three-dimensional CFD software that is capable of employing highly refined computational meshes. It models liquid fuel evaporation, transport of fuel vapor, oxygen and other relevant species, reaction and heat release, soot and intermediate species formation/destruction, diffuse radiation within the fire, and radiation view factors from the fire edge to nearby objects and the surroundings.

ISIS-3D employs semiempirical combustion chemistry and radiation heat transfer models for large pool fires. These models are theoretically based but use parameters whose values are determined based on measurements made in fires whose size and other conditions are relevant to risk studies. For example, the radiation model divides the computational domain into a diffusely radiating fire and its nonparticipating surroundings. It is therefore only valid for smoky fuels (such as JP-8) in pools with diameters greater than 2 m [4].

These models enable ISIS-3D to give engineering level accurate heat transfer results for fire environments that are relatively 'close' to those for which the parameters were determined, even when relatively coarse computational grids are employed. ISIS-3D is not intended for use far from those environments (i.e., different fuel types or fires with nondiffusive radiation transport). Moderate resolution ISIS-3D simulations ($< 60{,}000$ nodes) are relatively fast running and hence well suited for risk assessment studies. Scoping studies performed with ISIS-3D calculations may be complemented with highly refined CFD fire simulations for selected conditions.

One-dimensional transient conduction modules are also embedded in ISIS-3D. These modules allow the software to calculate the response of simple solid objects to the fire heat transfer without affecting the CFD time step. The three-dimensional container analysis fire environment (CAFE-3D) is a related computer software that allows the flowing medium modeled by ISIS-3D to be linked to commercial finite element programs [5,6], such as ANSYS or PATRAN. In CAFE-3D, the finite element program is used to calculate the detailed three-dimensional response of complex objects (such as a nuclear waste transport package) to a fire.

ISIS-3D simulations have been benchmarked against experiments that measure the response of large pipe calorimeters to hydrocarbon pool fires [7,8]. These works show that ISIS-3D accurately reproduces measurements for different calorimeter sizes and placements relative to the fuel pool, and for a variety of wind conditions. The purpose of the current work is to describe the semiempirical combustion chemistry and radiation heat transfer models employed in ISIS-3D, and the methods used to determine the parameter values.

ISIS-3D

This section describes the numerical and modeling methods used in the ISIS-3D CFD/diffuse radiation computer software. ISIS-3D solves the three-dimensional mass, momentum (Navier–Stokes), energy, and species transport equations using a variable density version [9] of the PISO [10] pressure-based solution algorithm. It models turbulence using Reynolds averaged Navier–Stokes approach with eddy diffusivity dependent on local velocity gradients and the computational cell size [11,12]. This approach is similar to large eddy simulations (LES) except that the computation cell sizes are typically larger.

ISIS-3D uses a finite volume method with an orthogonal grid for discretizing the governing equations. In this formulation all vector quantities, such as heat flux and momentum, are defined at the cell interfaces whereas scalar variables, such as temperature and pressure, are defined at cell centers. Applying finite volume discretization with an orthogonal grid is closely related to a finite difference approach.

ISIS-3D uses a porosity method similar to the fractional area volume obstacle representation [13] method for representing curved surfaces. This method admits a flat diagonal surface within a hexahedral finite volume computational cell. Multiple cells with diagonal interior surfaces are used to represent a curved object, such as a cylinder. This representation is much more accurate than the stair step technique that is often used in finite difference simulations. A segmented object representation has an equivalent heat transfer and flow representation as a finite element CFD method, but it does not incur the increased processor and memory requirements associated with finite element methods. With the porosity method, the flow areas on all cell surfaces are adjusted to account for the diagonal solid surface. Heat transfer takes place between the flowing medium and the solid in the same computational cell through the diagonal surface.

One-dimensional transient conduction modules are also embedded in ISIS-3D. Either or both 'ends' of each module are coupled to the flowing medium region and used to model the response of objects engulfed in or near the flames. They allow conduction within fine scale objects to be modeled without affecting the CFD time step.

In some cases, the advection and thermal time scales of the flowing (fire) medium are much smaller than the relevant time scales of the engulfed solid object. Under these conditions, the specific heat of all the solid region materials can be reduced by a common factor. This effectively speeds up the solid object response and allows the total computational time to be reduced. In the current work, simulations are performed with an acceleration time factor of $TF = 12$. To do this, the specific heat of the solids are reduced by a

factor of twelve, the simulation is preformed for only one-twelfth the real fire duration, and the time scale is multiplied by a factor of twelve. This technique greatly increases the number of simulations that can be performed in a given time. It will be seen that this time dilation technique has only a small effect on the predicted total energy transferred from a fire to an object. However, it can only be used if the wind conditions are changing slowly [8].

Radiation Heat Transfer Model

High volume fractions of soot within large fires make them optically thick and radiatively diffuse [14]. Within the flowing region of the computational domain, ISIS-3D employs different techniques to model heat transfer inside and outside the flame zone. The flame zone is defined as computational cells where the soot volume fraction f_S is above a user-defined minimum value, $f_{S,m}$. As $f_{S,m}$ decreases, the effective fire size calculated by ISIS-3D increases and its surface emission decreases. The value of $f_{S,m}$ is based on measurements from a large fire heat transfer experiment. The method for choosing $f_{S,m}$ is described later in this article.

The fire interior (where $f_S > f_{S,m}$) is assumed to be optically thick and radiation transport is diffuse [14]. Diffuse radiation within the fire is modeled indirectly using the Rosseland conduction approximation. This approximation employs an effective, temperature-dependent thermal conductivity of the flowing medium equal to

$$k_R = \frac{16n^2\sigma T^3}{3\beta} \tag{1}$$

In this expression, σ is the Stephan–Boltzmann constant, β is the local extinction coefficient of the medium, n is the index of refraction, and T is the local soot and gas temperature. The soot particles are of submicron size and hence their temperatures are assumed to be the same as the surrounding gas. The extinction coefficient is a function of the local mass fractions of soot, water vapor, fuel vapor, and intermediate species [14]. The Rosseland conductivity within the fire is much larger than the molecular values for air.

The optically thick assumption is not applicable to computational cells that are in contact with solid or liquid surfaces or at the edge of the flame zone. Heat transfer from the fire to the environment and to the engulfed surfaces is calculated based on the temperature of those bodies and the temperature of the fire cell adjacent to them. Steep temperature gradients near bounding surfaces cause the Rosseland conduction approximation to overestimate heat flux and underestimate bounding surface temperatures. A jump boundary condition [14,15] at bounding surfaces has been applied

by many investigators to overcome these problems. In ISIS-3D, jump boundary conditions are created by applying a volumetric heat source term at bounding surfaces equal to:

$$Q_{\mathrm{v}} = \frac{\sigma A(T^4 - T_{\mathrm{w}}^4)}{((3\beta\Delta/4) - (1/\varepsilon_{\mathrm{w}}))V} \tag{2}$$

In this expression, T is the gas/soot temperature at the surface, T_{w} is the solid surface temperature, β is the local extinction coefficient, Δ is the distance between the cell centroid and the surface, ε_{w} is the surface emissivity, A is the surface area of the material within or adjacent to the cell, and V is the volume of the cell.

Outside the flames (where $f_{\mathrm{S}} < f_{\mathrm{S,m}}$), the gaseous medium does not participate in radiation heat transfer. The outer edge of the flame zone radiates heat to the environment as well as solid surfaces. ISIS-3D performs a view factor calculation between all points on the fire outer surface to all points on the objects defined in the computational domain. This calculation neglects the shadowing effects from the irregular fire surface to reduce the computational expense. The heat transfer calculation assumes the flame outer surface is optically black, $\varepsilon_{\mathrm{FireSurface}} = 1$.

In the current work, heat loss to the surroundings is calculated based on an environment temperature of $T_{\mathrm{Environment}} = 400\,\mathrm{K}$. Simulations employing $T_{\mathrm{Environment}} = 300$ and $500\,\mathrm{K}$ give very similar results. All solid surfaces radiate to the environment when they are not engulfed in flames. Here, a view factor of 0.56 is applied whenever a surface is not engulfed, and it does not vary with location or time. Newer versions of ISIS-3D calculate the view factor at each location and at each time step, at a very small computational cost. Results from the newer versions are in good agreement with simulations that use the 0.56 view factor.

Combustion Chemistry Model

The combustion chemistry model in ISIS-3D is defined by the user through an input file so that it can be varied as desired for different fuels. In the course of making numerous benchmarking calculations, we have developed a simplified combustion chemistry model for JP8 jet fuel that reproduces heat transfer and temperature results for a wide range of pool fire simulations. This combustion chemistry model has some of the features found in detailed fire models, yet is simple enough to be computationally inexpensive. It is not intended to produce or track multiple intermediate chemical species of combustion nor the formation of pollutants. Instead, the model is focused upon heat transfer and thermal effects.

The combustion model uses four separate reactions to represent the chemical processes within a JP8 hydrocarbon pool fire. This model is a variant of a turbulent flame model developed by Said et al. [16]. It is a fast-running empirical model that includes soot production from normal combustion and anaerobic fuel cracking, soot oxidation, as well as feedback to the reaction chemistry through species and energy transport.

The relevant species in this model are the hydrocarbon fuel vapor (denoted as F), atmospheric oxygen (O_2), solid carbon soot (C), an intermediate species (IS), and products of complete combustion (PC, which consist of CO_2 and H_2O vapor). The radiative properties of both the fuel F and the intermediate species IS are assumed to be the same as that of methane.

The first reaction is incomplete fuel combustion that produces carbon soot in addition to the products of complete combustion. The combustion soot parameter S_1 describes the mass of soot produced per unit mass of fuel consumed in this reaction. The mass-based functional formula for this reaction is:

$$1\,\mathrm{kg\,F} + (3.0 - 2.6\,S_1)\,\mathrm{kg\,O_2} \rightarrow S_1\,\mathrm{kg\,C} + (4.0 - 3.6\,S_1)\,\mathrm{kg\,PC} + (42 - 32\,S_1)\,\mathrm{MJ} \tag{3}$$

One of the differences between the current combustion chemistry model and the one presented by Said et al. is that they assume that when fuel reacts with oxygen, it does not produce soot ($S_1 = 0$). As S_1 increases, soot production from this reaction increases, the amount of normal products of combustion decreases, and the heat of reaction goes down.

The second reaction is endothermic fuel cracking. This reaction is anaerobic and produces soot and intermediate species. The cracking soot parameter S_2 describes the mass of soot this reaction produces per mass of fuel it consumes as follows:

$$1\,\mathrm{kg\,F} + 0.3\,\mathrm{MJ} \rightarrow S_2\,\mathrm{kg\,C} + (1 - S_2)\,\mathrm{kg\,IS} \tag{4}$$

In this reaction, 0.3 MJ of heat is consumed for every kilogram of fuel that it reacts with. The third reaction is carbon soot combustion. The chemical formula for this reaction is:

$$1\,\mathrm{kg\,C} + 2.6\,\mathrm{kg\,O_2} \rightarrow 3.6\,\mathrm{kg\,CO_2} + 32\,\mathrm{MJ} \tag{5}$$

The final model reaction is combustion of the intermediate species.

$$1\,\mathrm{kg\,IS} + \frac{3 - 2.6S_2}{1 - S_2}\,\mathrm{kg\,O_2} \rightarrow \frac{4 - 3.6S_2}{1 - S_2}\,\mathrm{kg\,PC} + \frac{41.7 - 32S_2}{1 - S_2}\,\mathrm{MJ} \tag{6}$$

The coefficients in this reaction are determined such that complete combustion of the intermediate species and soot produces the same species and thermal energy as direct combustion of the fuel.

The Arrhenius rate model is used for all four reactions. As such, the consumption of fuel, soot, and intermediate species are described by

$$\frac{\mathrm{d}f_{R_1}}{\mathrm{d}t} = -C\left[\prod_i^N f_{R_i}\right] e^{-T_A/T} \tag{7}$$

In this expression, N is the number of reactants for a given reaction. The mass fraction of each reactant is f_{R_i} for $i=1$ to N, C is the preexponential coefficient for the reaction, and T_A is the effective activation temperature for the reaction. We see that the local rate of mass consumption of the primary reactant (per unit mass within a control volume) $\mathrm{d}f_{R_1}/\mathrm{d}t$ increases with the local absolute temperature T and the product of all the local reactant mass fractions. The primary reactant R_1, the number of reactants N, and the effective activation temperature T_A for each reaction are given in Table 1. The effective activation temperatures in Table 1 for the fuel cracking and soot combustion reactions were taken from Said et al. [16]. The values of T_A for the other reactions were set to low values so that they are limited only by diffusion and turbulence.

Combustion Chemistry Parameter Selection

There are six remaining parameters in the reaction chemistry model. They are the combustion and cracking soot parameters, S_1 and S_2, and the preexponential coefficient C for the four reactions. In the current work, these values were determined by comparing results calculated by ISIS-3D with experimental data measured by Gritzo et al. [17]. That experiment employed a 6-m square JP8 pool fire. The soot temperature and soot volume fraction were measured at one location as a function of time under low wind conditions.

Table 1. Combustion chemistry model rate parameters used in ISIS-3D.

Reaction	R_1	N	T_A (K)	C
Fuel combustion	F	2	8000	10^{13}
Fuel cracking	F	1	42,730*	10^{14}
Soot combustion	C	2	26,500*	10^{8}
Intermediate species combustion	IS	2	8000	10^{13}

*Value from Said et al. [16].

In the current work, ISIS-3D simulations of the same fire geometry and conditions were performed for a range of preexponential coefficients and soot parameters. The probability distribution functions (PDFs) of the measured soot temperature and soot volume fraction were compared with the ISIS-3D-calculated distributions to determine parameters that gave results closest to the measured data.

Figure 1(a) and (b) shows probability distribution functions for soot temperature and soot volume fraction, respectively. The soot temperature

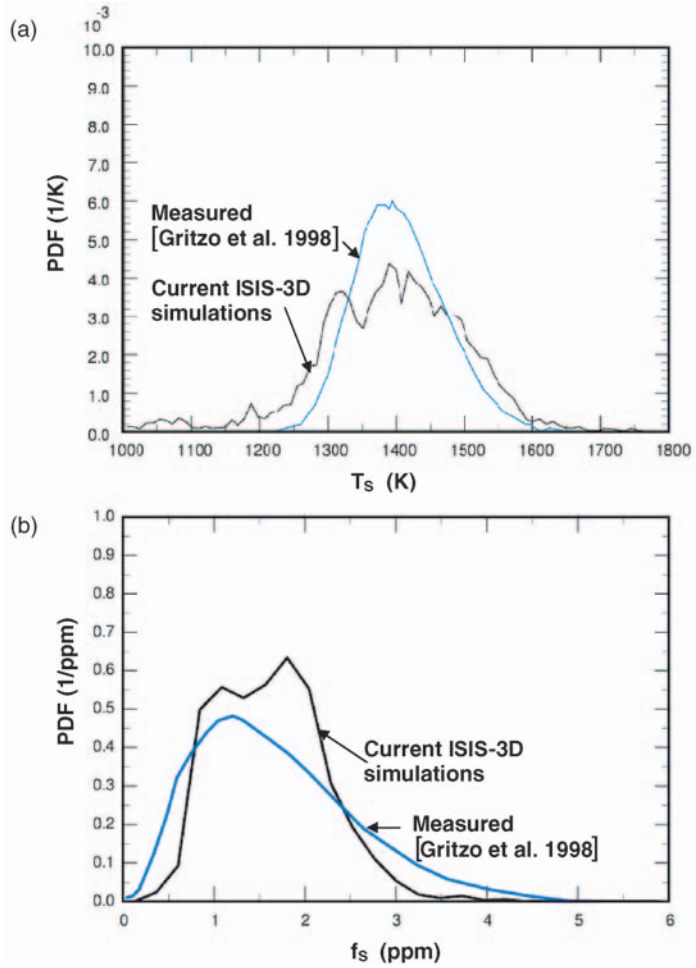

Figure 1. *Measured [17] and ISIS-3D simulated probability density functions (PDF) for (a) soot temperature and (b) soot volume fraction. (The color version of this figure is available on-line.).*

with the highest measured probability was roughly 1400 K, and the most probable measured soot volume fraction was $\approx$1.2 ppm (1.2×10^{-6}). The ISIS-3D-calculated distributions shown in Figure 1 use the preexponential coefficients presented in the last column of Table 1 and the soot parameters $S_1 = 0.05$ and $S_2 = 0.15$. This set of parameter values gave the closest agreement with the experimental distributions of all the sets considered in this work.

The calculated distributions are not identical to the measured ones, but they are similar and peak at nearly the same temperature and volume fraction. These parameters were therefore used in all subsequent ISIS-3D simulations. In this work, an implicit assumption is made that the soot parameters and preexponential coefficients are not functions of wind speed or pool size. However, additional soot data from other experiments will allow a functional dependence to be determined.

FIRE TESTS

Nine experiments were performed by other investigators to measure the thermal response of a 3.66-m-diameter culvert pipe suspended near the leeside of 9.5- and 19-m-diameter JP8 fuel pools under a variety of wind conditions [18]. The pipe interior temperature and wind conditions upwind of the facility were measured as functions of time. This section describes the test facility, wind conditions, and pipe temperatures of one of those tests (Experiment 3). ISIS-3D simulations of that test are described in the next section for different values of $f_{S,m}$ (which is the soot volume fraction ISIS-3D used to define the edge (size) of the diffusely radiating fire region). The simulated pipe temperatures are then compared to the measured data to determine the most appropriate value of $f_{S,m}$.

Facility

Figure 2(a) shows a plan view of the test facility. The circle represents an 18.9-m diameter pool in which JP8 aviation fuel floated on the top of the water. An arrow shows the 'predominant' wind direction at the site. A 3.66-m (12 ft) diameter, 18.28-m (60 ft) long culvert pipe, with 1.6 cm (0.063 in.) thick mild steel walls, is suspended 0.3 m above the leeward edge of the pool. Its axis is perpendicular to the predominant wind direction. The z-axis is aligned with the pipe axis and the x-axis is aligned with the predominant wind direction. The angle θ is measured clockwise from the x-axis.

The wind speed and direction were measured at six different locations upwind of the fire zone. The anemometers were placed at three elevations, 1.83, 5.5, and 9.1 m (6, 18, and 30 ft) above the ground on two poles.

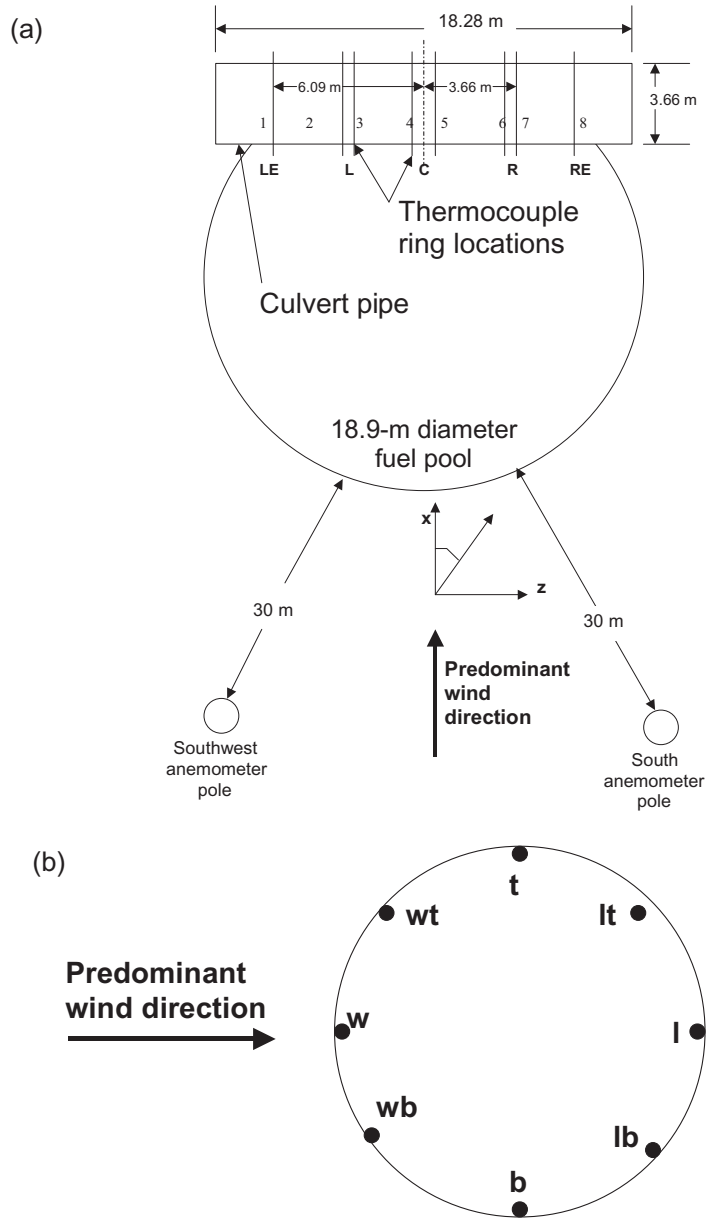

Figure 2. *Fire test facility [18]: (a) plan view showing pipe calorimeter, fuel pool, anemometer pole locations, and reference axes and (b) elevation section view showing calorimeter thermocouple locations.*

Figure 2(a) shows the poles were located 30 m south and southwest of the fuel pool.

The pipe interior temperature was measured at 56 locations using thermocouples. These thermocouples were equally spaced around eight different rings. In Figure 2(a), lines on the pipe labeled 1 to 8 show the approximate axial locations of these rings. Rings 4 and 5 were 0.6 m (2 ft) apart and located roughly halfway between the two pipe ends. These two rings together are referred to as the central rings, and they are marked with the letter C. Left-side rings (labeled 2 and 3, and together L) and right-side rings (6 and 7, and together R), were roughly 3.66 m (12 ft) on either side of the central rings. A left-end ring (labeled 1 and LE) and a right-end ring (8 and RE) were 6.09 m (20 ft) on either side of the central location.

Figure 2(b) shows an elevation section view of the pipe. It indicates the angular position of the thermocouples relative to the predominant wind direction. Rings 1 and 8 had only four thermocouples at positions w (windward), t (top), l (leeward) and b (bottom). Rings 2–7 had thermocouples at all eight positions including the wb (windward bottom), wt (windward top), lt (leeward top), and lb (leeward bottom) positions. The 1.6-mm-diameter thermocouples were held to the pipe using 0.3-mm-thick nichrome strips that were spot welded to the interior surface. The thermocouples were backed with 25.2-mm-thick fiber insulation.

Experimental Results

The thermocouple data for this experiment indicate that the burn duration was roughly 670 s (11.2 min). Figure 3(a) and (b) shows the wind direction and speed measured by the anemometers at the 1.87-m and 9.1-m elevations on the south and southwest anemometer poles (color versions of the figures are available in the on-line edition of this article). Data from the 5.5-m elevation anemometers had a systematic time shift compared to the other measurements and were therefore not used in the current work. The average direction and speed were roughly -11° (slightly to the left of the predominant wind direction in Figure 2(a)) and 9.5 m/s (25 m/h), respectively. The wind direction and speed exhibit rapid variations with time, but neither exhibited significant sustained (low frequency) shifts.

Figure 4 shows the measured thermocouple temperatures during the fire. Figure 4(a) shows the data from the central regions of the pipe (rings 2–7). In the simulations described in the next section, the computational grid was not sufficiently refined to resolve the difference between ring pairs 2 and 3 (the left rings, L), 4 and 5 (the central rings, C), and 6 and 7 (the right ring, R). In Figure 4(a), the data with the prefix C are an average of the measured data from rings 4 and 5, and the suffixes indicate the

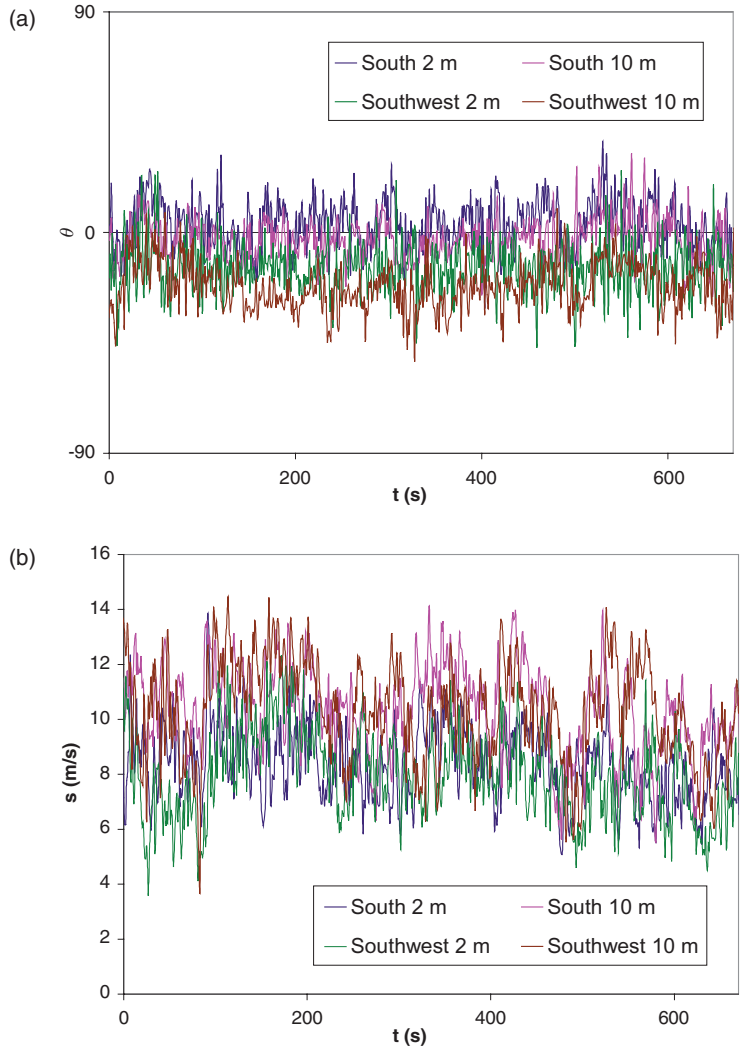

Figure 3. *Wind conditions vs time measured by four anemometers during fire test burn period [18]: (a) wind direction and (b) wind speed. (The color version of this figure is available on-line.)*

angular location (as seen in Figure 2(b)). This averaging is used so that the experimental data can be easily compared to the simulation results. Similarly, the prefix L indicates the data averaged from rings 2 and 3, while the average of rings 6 and 7 are labeled with prefix R. The data from all

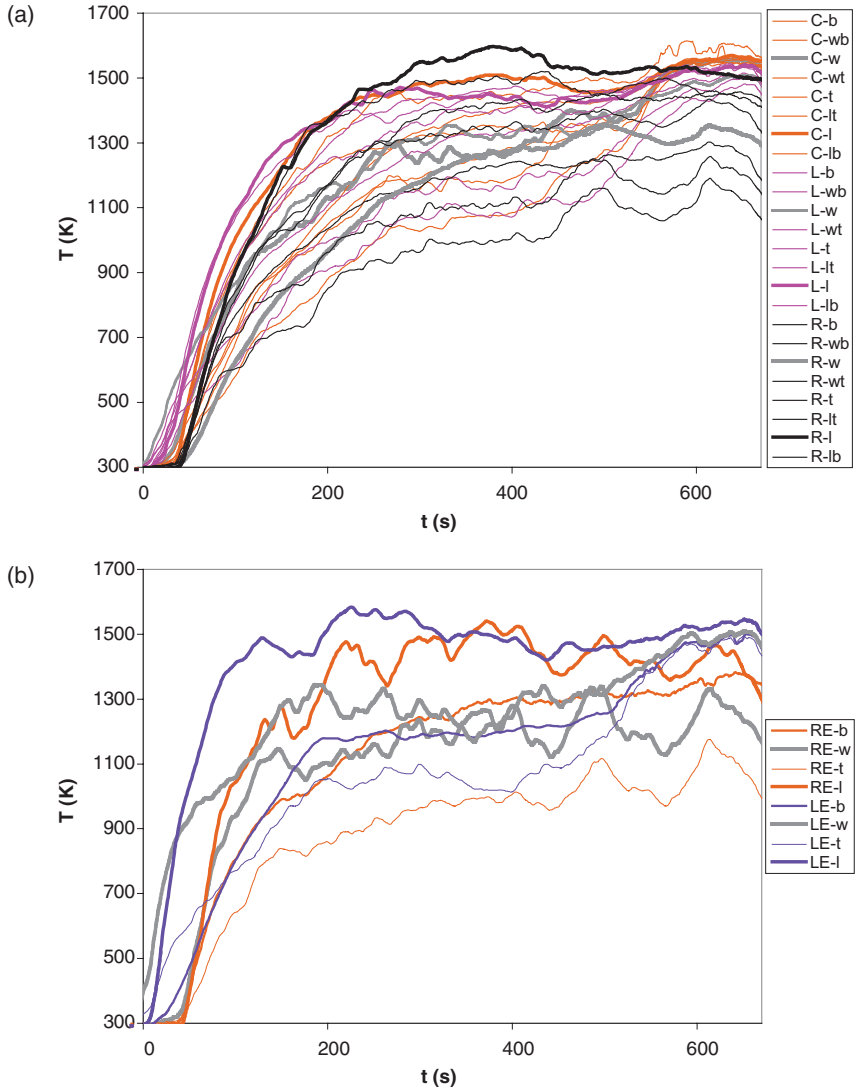

Figure 4. *Thermocouple temperatures measured during fire test burn period [18]: (a) central rings L, C, and R and (b) end rings LE and RE. (The color version of this figure is available on-line.)*

eight thermocouples from the left-end (LE) and right-end (RE) rings are included in Figure 4(b) without any spatial averaging.

All thermocouples were roughly 300 K before the test began. The temperatures did not begin to rise at the same time. Presumably this is

because the fire started at discrete locations and required time to spread and cover the pool. The temperature of all the thermocouples rose until roughly $t = 300$ s when they reached steady state conditions. The highest and lowest temperatures were roughly 1600 and 1000 K. Finally, the temperatures on the central and left-hand rings (rings C, L, and LE) began to increase at time $t \cong 450$ s, and they became nearly uniform at 1500 K after $t = 600$ s. Surprisingly however, the wind data in Figure 3 do not exhibit any sustained shifts during that time period.

Figure 5 shows the angular variation of temperature at time $t = 400$ s for each ring. Figure 4 shows that the temperatures are relatively steady at that time. The highest temperatures are observed on the leeward side of the pipe, and the lowest temperatures are on the upper windward region. The strong winds that were present during this test tilted the flames so that the leeward pipe surface was more continuously engulfed in flames than the windward side. Moreover, a recirculation zone may have developed downwind of the pipe. Enhanced air/fuel mixing in such a zone may increase the fire temperatures, which would contribute to the high temperatures observed on

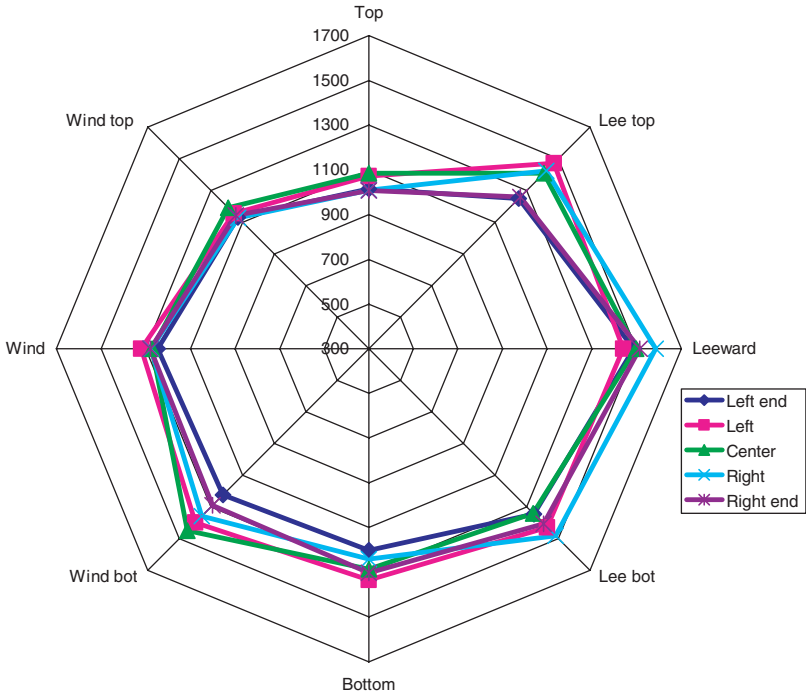

Figure 5. *Angular variation of thermocouple temperature for all five rings, measured at $t = 400$ s during the fire test [18]. (The color version of this figure is available on-line.)*

the leeward pipe surface. Finally, the temperatures are nearly the same at each axial position.

FIRE SIMULATIONS

Computational Domain and Boundary Conditions

Figure 6 shows the computational domain and grid used in the ISIS-3D simulations of the experimental conditions. The x, y, z-coordinate axes are also defined. The rectangular domain is 60, 15, and 60 m in the x-, y-, and z-directions. The 18.28-m-long, 3.66-m-diameter pipe, and the 18.9-m-diameter pool are also shown in Figure 6. The pipe axis is aligned with the z-axis and the predominant wind moves in the x-direction. These directions are consistent with the coordinates used in Figure 2(a). The computational grid uses 31, 19, and 28 volumes, respectively, in the x-, y-, and z-directions. The grid is more highly refined near the pipe than it is near the domain boundaries.

The grid on the pipe indicates the locations of different surface elements. Each element is linked to a one-dimensional conduction module. The local heat transfer from the fire to each surface element is dependent on the surface element temperature. At each time step, the local heat transfer to a surface element is used as a thermal boundary condition for its conduction module. The modules simulate transient conduction through the 1.6-mm thick steel pipe wall, the 1.6-mm thick thermocouple bead, a 0.1-mm air gap,

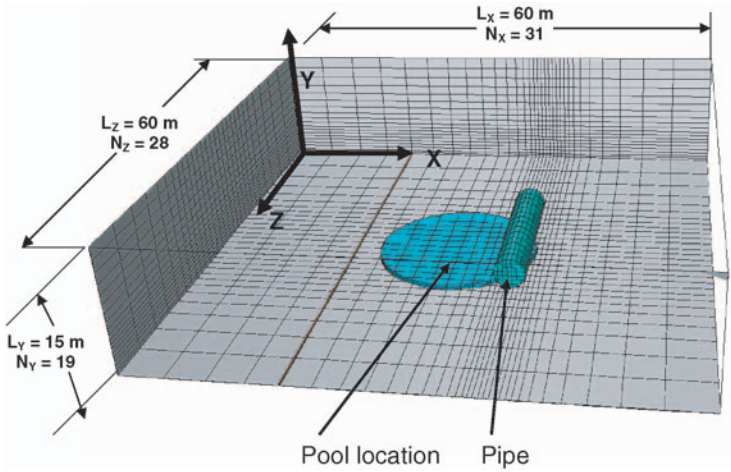

Figure 6. *ISIS-3D computational domain and mesh used for fire test simulations. (The color version of this figure is available on-line.)*

the 0.3-mm nichrome strap that holds the thermocouple to the interior pipe surface, and the 25.4-mm thick insulation. The surface element temperature is updated at each time step and used as a thermal boundary condition for the fire simulation. This method models conduction in the radial direction of the thin walled calorimeter but neglects the azimuthal and axial components. Moreover, even though the thermocouples and nichrome straps in the experiment were placed at discrete locations, the simulation models them as though they are uniformly spread over the interior surface of the pipe.

The thermocouple bead temperatures at the locations shown in Figure 2 are outputs of the simulations. As mentioned earlier, the surface grid in Figure 4 is not sufficiently refined to resolve the difference between the closely spaced ring pairs 2 and 3 (the left rings, L), 4 and 5 (the central rings, C), and 6 and 7 (the right ring, R). As a result, the software reports only one temperature at each of the eight azimuthal locations on rings L, C, and R.

The measured wind conditions were applied to the upwind surfaces of the computational domain. The wind measurements acquired by both anemometers at the 1.8-m-elevation were vector averaged and applied in the region $y = 0$–6 m. Similarly, the data measured at $y = 9.1$ m were applied to the region $y = 6$–15 m. These velocities were applied on the upwind wall (at $x = 0$) and on the upwind halves ($x = 0$ to $L_x/2$) of the front and back walls at $z = 0$ and L_z. Hydrostatic pressure boundary conditions were applied to the remaining sidewalls and the top boundary. We note that wind data from only four widely separated upwind locations were used to derive the computational velocity boundary conditions and no wind data were available downwind of the fire. Such sparse data is typical of fire tests but makes it difficult to completely characterize the fire's environment.

No-slip velocity conditions are applied to all locations on the bottom boundary of the domain except for the fuel pool. The 18.9-m-diameter pool is divided into two regions: an interior 16.9-m-diameter circle, and an outer 1-m-wide ring that covered the remainder of the pool. Constant fuel injection rates of 0.055 and 0.185 kg/(m^2 s) are applied to the inner circle and the outer ring. These conditions lead to an average evaporation rate of 0.072 kg/(m^2 s), which is typical of large hydrocarbon pool fires [19]. The larger rate for the outer ring is intended to model high levels of heat transfer and entrainment that occur at the pool edge. However, the relative size and evaporation rates of the two regions are somewhat arbitrary.

Radiation Heat Transfer Parameter Selection

Figure 7 shows the average thermocouple temperature rise ΔT_{avg} as a function of time. This rise is the difference between the average

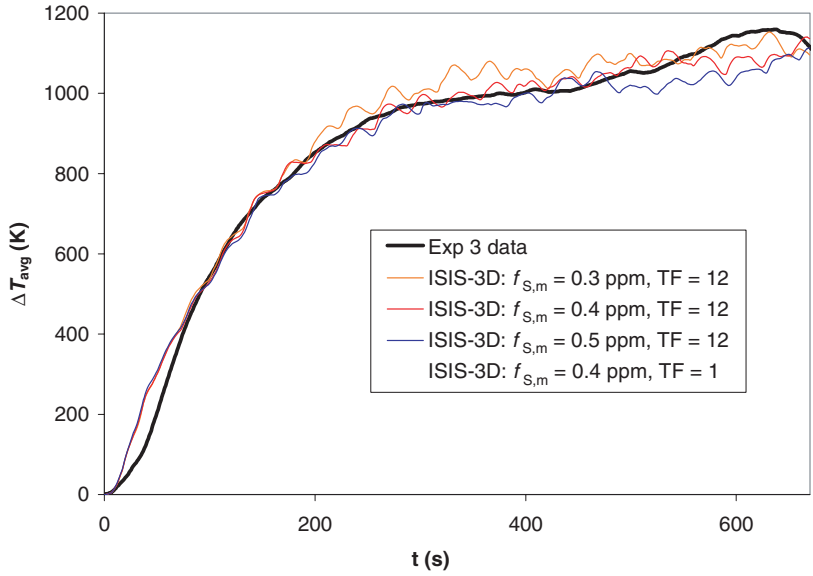

Figure 7. *Average thermocouple temperature rise vs time from fire test [18] and ISIS-3D simulations. (The color version of this figure is available on-line.)*

thermocouple temperature at a given time and its value at the start of the test ($t = 0$). It is an indication of the total energy delivered to the pipe from the fire as a function of time. Risk analysis tools must accurately predict the total heat transfer to an object to determine if interior components reach their limit temperatures [20,21]. Both experimental data and results from ISIS-3D simulations are included.

The experimental temperature rise increases slowly for the first 40 s of the test. This may be due to the slow spread of the fire across the fuel pool. The experimental average temperature then increases rapidly until $t = 300$ s. From $t = 300$ to 450 s, the average temperature rise is fairly constant at $\Delta T_{\text{avg}} = 1000$ K. It then increases to roughly $\Delta T_{\text{avg}} = 1150$ K. This secondary rise is consistent with the late increase in local temperatures on the left and central regions of the pipe observed in Figure 4. The measured wind conditions in Figure 3 do not exhibit any sustained changes during this time. They therefore do not appear to be the cause of the secondary rise.

Results for accelerated simulations with TF = 12 are presented in Figure 7 for $f_{\text{S,m}} = 0.3$, 0.4, and 0.5 ppm. One real time simulation (TF = 1) is also reported with $f_{\text{S,m}} = 0.4$ ppm. All the simulations followed the general experimental behavior during the time period $80\text{ s} < t < 450\text{ s}$. Before this

time period, the average temperatures from the simulations rose more rapidly than that from the experiment. This is because the simulated fire grew uniformly over the fuel pool, but the experimental fire spread across the fuel pool before it grew upward. After $t = 450$ s, the simulations did not display the secondary temperature rise exhibited by the experiment because the wind data in Figure 3 did not exhibit any sustained changes.

All three of the accelerated simulations (TF = 12) display large amplitude oscillations in the average temperature rise. These simulations employ pipe and thermocouple specific heats that were reduced by a factor of twelve below the physical values. This artificial reduction causes the pipe temperatures to overrespond to the unsteady fire puffing, and leads to the oscillations. As $f_{S,m}$ decreases, the effective fire volume increases. This causes the fire to more continuously engulf the pipe. This increases the total energy delivered to the pipe and its average temperature rise. The value $f_{S,m} = 0.4$ ppm brought the simulation result closer to the experimental data than the other two values.

The average temperature rise from the TF = 1 simulations for $f_{S,m} = 0.4$ ppm was very similar to that from the TF = 12 calculation except that it did not exhibit the large amplitude oscillations. The average temperature rise predicted by the TF = 1 simulation is also very close to the experimental data. The parameter value $f_{S,m} = 0.4$ ppm was used in all subsequent calculations in this article.

The TF = 12 simulations required roughly 3.5 h to complete on a 2.4 GHz LINUX workstation with 0.5 Gb of RAM. The TF = 1 calculation required roughly 42 h on the same machine. Time acceleration appears to be a useful method for rapidly understanding the behavior of different fire models. Real time simulations are slower but useful for confirming selected results.

Local Temperature Results

Figure 8 is a snapshot of the fire region outer surface at $t = 400$ s. It is taken from the real time (TF = 1) simulation that employed $f_{S,m} = 0.4$ ppm. The surface is defined at the locations where the soot volume fraction $f_S = f_{S,m} = 0.4$ ppm, and it is shaded according to its local temperature. The pipe is the horizontal cylinder that is mostly engulfed in the fire. The fuel pool is located in front and to the left of the pipe, and the wind blows from the lower left of the figure toward the upper right.

A series of fire surface images shows that the fire rises up from all locations of the pool at the beginning of the fire and then engulfs the pipe.

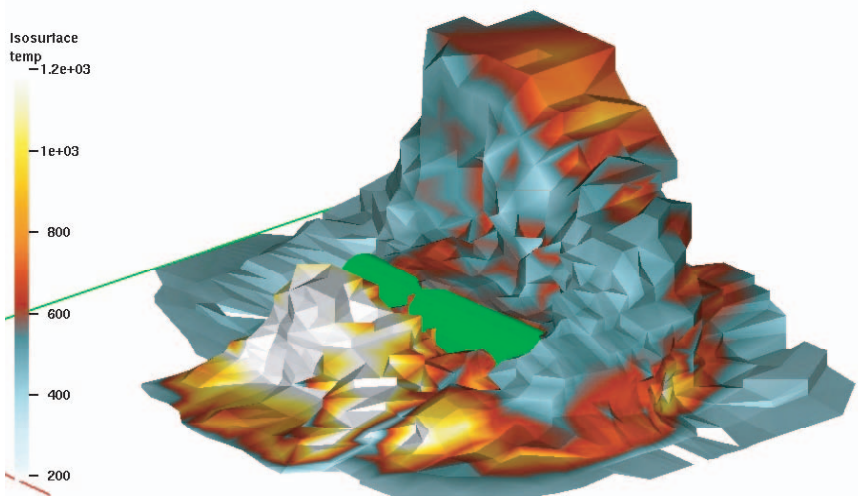

Figure 8. *Flame surface represented by a soot volume fraction equal to 0.4 ppm from a real time (TF = 1) ISIS-3D simulation of the fire test at time t = 400 s. The surface is shaded according to its local temperature in Kelvin. (The color version of this figure is available on-line.)*

After engulfment, the surface exhibits large-scale puffing. The fire volume is not fully contained in the computational domain and exits through the boundary on the right side. Finally, the surface in Figure 8 is fairly typical of other times during the simulation.

Figure 9 shows individual thermocouple temperatures versus time from the real time (TF=1) simulation with $f_{S,m} = 0.4$ ppm. Figure 9(a) shows data from the central rings, L, C, and R, and Figure 9(b) shows results for the left-end and right-end rings, LE and RE. At any given time, the range of temperatures in the simulations is similar to those of the experiment, shown in Figure 4. However, the temperature at each simulated location is not the same as the measured values.

Figure 10 shows the variation of temperature with angular position at $t = 400$ s from the real time simulation with $f_{S,m} = 0.4$ ppm. Results are given for all five axial locations. The results are fairly uniform at each axial position, and the maximum temperatures are on the leeward side of the pipe. These characteristics are similar to those of the experimental data shown in Figure 5. While the highest measured temperatures are located on the upper portion of the leeward side, the highest temperatures from the simulations are nearer to the ground. The simulated local calorimeter temperatures are similar to the measured values even though the heat transfer parameter $f_{S,m}$ was determined based on the average temperature rise.

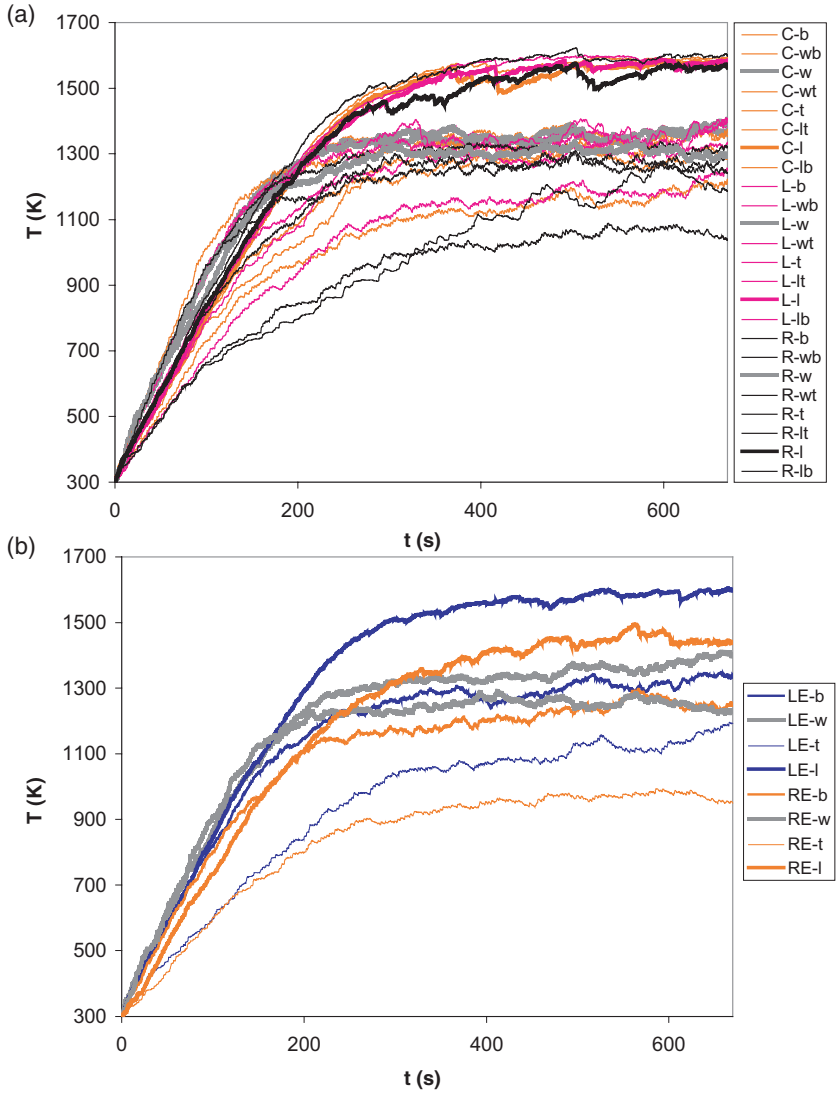

Figure 9. *Local thermocouple temperatures vs time from a real time (TF = 1) ISIS-3D fire test simulation with $f_{S,m} = 0.4$ ppm: (a) central rings L, C, and R, and (b) end rings LE and RE. (The color version of this figure is available on-line.)*

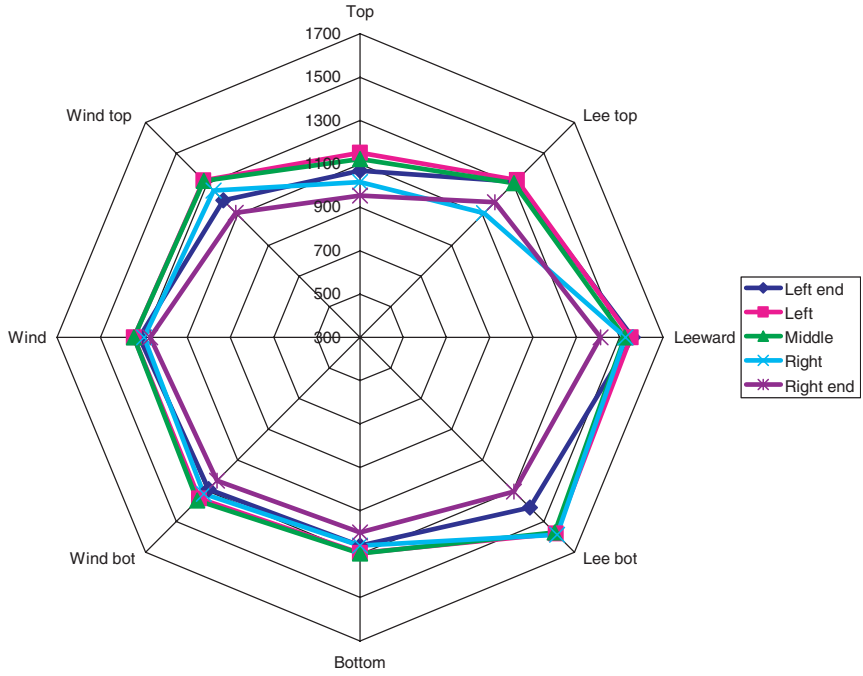

Figure 10. *Angular variation of thermocouple temperature for all five rings at $t = 400$ s from a real time ($TF = 1$) ISIS-3D fire test simulation with $f_{S,m} = 0.4$ ppm. (The color version of this figure is available on-line.)*

CONCLUSIONS

The ISIS-3D CFD/radiation heat transfer computer software simulates heat transfer from large pool fires to engulfed packages for risk studies. These studies require accurate estimates of the total heat transfer to an object and the general characteristics of the object temperature distribution for different wind environments and placement of the package relative to the fuel pool. Since risk studies require multiple simulations, their analysis tools must be rapid as well as accurate. To meet these needs, ISIS-3D employs semiempirical reaction rate and radiation heat transfer models that allow it to accurately model large-fire heat transfer even when relatively coarse computational grids are employed. These models employ parameters whose values are selected based on large fire experiments.

In the current work, parameters for the reaction rate model are selected based on comparison with soot volume fraction and temperature measurements acquired in a recent 6-m square pool fire under light wind conditions.

The soot volume fraction ISIS-3D uses to define the edge of the optically thick fire is determined using the measured average temperature rise of a pipe engulfed in a 19-m-diameter pool fire with a steady 9.5 m/s crosswind. The simulations accurately predicted the spatial and temporal variation of the pipe without further adjustments. Accelerated simulations, in which the specific heat of the engulfed pipe was reduced by a factor of twelve below the measured values, simulated the 11-min crosswind fire in a few hours on a standard desktop workstation. These simulations accurately reproduced the character of this fire even though wind data from only four upwind locations were used to derive the velocity boundary conditions.

Since the reaction rate and radiation heat transfer models have been validated against only a few experiments, ISIS-3D cannot be considered a fully predictive simulation at present. It can be used with confidence to interpolate between conditions where it has been validated. Future work will compare ISIS-3D results to experiments for a range of pool sizes and under a range of wind conditions.

NOMENCLATURE

C = reaction rate preexponential coefficients
$f_{S,m}$ = soot volume fraction at flame boundary $= 0.4 \times 10^{-6}$ (0.4 ppm)
f_S = soot volume fraction
$L_x L_y L_z$ = domain dimensions
N = number of reactants
$N_x N_y N_z$ = number of cells in x-, y-, and z-directions
s = wind speed
S_1, S_2 = soot formation parameters
t = time
T = temperature
T_A = effective activation temperature
$T_{Environment}$ = environment temperature = 400 K
T_w = wall temperature
V = cell volume
x, y, z = Cartesian coordinates
ΔT_{avg} = average thermocouple temperature rise
β = local extinction coefficient
θ = wind direction
σ = Stephan-Boltzmaan constant
$\varepsilon_{FireSurface}$ = fire surface emissivity = 1

ACKNOWLEDGMENTS

This work was supported by the Defense Threat Reduction Agency (DTRA) through a Small Business Innovative Research project, contract number DTRA01-01C-0084 (Phase II SBIR). It was also supported by the University of Nevada, Reno Faculty Development Leave Program.

REFERENCES

1. Fischer, L.E., Chou, C.K., Gerhard, M.A., Kimura, C.Y., Martin, R.W., Mensing, R.W., Mount, M.E. and Witte, M.C., "Shipping Container Response to Severe Highway and Railway Accident Conditions," NUREG/CR4829, 1987.
2. U.S. Nuclear Regulatory Commission, "Packaging and Transportation of Radioactive Material," Rules and Regulations, Title 10, Part 71, Code of Federal Regulations, 2000.
3. Lopez, A.R., Gritzo, L.A. and Sherman, M.P., "Risk Assessment Compatible Fire Models (RACFMs)," Sandia Report SAND97-1562, July 1998.
4. Murphy, J.J. and Shaddix, C.R., "Soot Properties and Species Measurements in a Two-Meter Diameter JP-8 Pool Fire: 2003 Test Series," Sandia Report Sand2004-8085, March 2004.
5. Lopez, C., Koski, J.A. and Suo-Anttila, A., "Development and Use of the CAFE-3D Code for Analysis of Radioactive Material Packages in Fire Environment," In: Presented at the 44th International Nuclear Material Management (INMM) Conference, 2003.
6. Suo-Anttila, A.J., Koski, J.A. and Gritzo, L.A., "CAFE: A Computer Tool for Accurate Simulation of the Regulatory Pool Fire Environment for Type B Packages," SAND99-0625C, March 1999.
7. Are, N., Greiner, M. and Suo-Anttila, A., "Benchmark of a Fast Running Computational Tool for Analysis of Massive Radioactive Material Packages in Fire Environments," to appear in *ASME J. of Pressure Vessel Technology*, 2005.
8. Greiner, M. and Suo-Anttila, A., "Validation of the ISIS Computer Code for Simulating Large Pool Fires Under a Variety of Wind Conditions," ASME J. Pressure Vessel Technology, Vol. 126, 2004, pp. 360–368.
9. Suo-Anttila, A., F2D Users Manual: A Two-Dimensional Compressible Gas Flow Code, Sandia National Laboratories Report, SAND92-7343, June 1993.
10. Issa, R.I., "Solution of the Implicitly Discretised Fluid Flow Equations by Operator Splitting," J. Comput. Phys., Vol. 62, 1985, pp. 40–65.
11. Smagorinsky, J., "General Circulation Experiments with the Primitive Equations," Monthly Weather Review, Vol. 91, 1963, pp. 99–165.
12. Ferzinger, J.H., "Subgrid-Scale Modeling," In: Galperin, B. and Orszag, S.A. eds., Large Eddy Simulations of Complex Engineering and Geophysical Flows, Cambridge University Press, Cambridge, 1993, pp. 37–54.
13. Hirt, C.W. and Sicilian, J.M., "A Porosity Technique for the Definition of Obstacles in Rectangular Cell Meshes," In: 4th International Conference on Ship Hydrodynamics Washington, DC, September 1985.
14. Modest, M.F., Radiative Heat Transfer, 2nd ed., Academic Press, New York, 2003.
15. Siegel, R. and Howell, J.R., Thermal Radiation Heat Transfer, Hemisphere Publishing Corporation, New York, 1981.
16. Said, R., Garo, A. and Borghi, R., "Soot Formation Modeling for Turbulent Flames," Combustion and Flame, Vol. 108, 1997, pp. 71–86.

17. Gritzo, L.A., Sivathaunu, Y.R. and Gill, W., "Transient Measurements of Radiative Properties, Soot Volume Fraction, and Soot Temperature in a Large Pool Fire," Combustion Science and Technology, Vol. 139, 1998, pp. 113–136.
18. Suo-Anttila, J.M. and Gritzo, L.A., "Thermal Measurements from a Series of Tests with a Large Cylindrical Calorimeter on the Leeward Edge of a JP-8 Pool Fire in Crossflow," Sandia National Laboratories Report, SAND2001-1986, June 2001.
19. Gritzo, L.A., Moya, J.A. and Murray, D., "Fire Characterization and Object Thermal Response for a Large Flat Plate Adjacent to a Large JP4 Fuel Fire," Sandia National Laboratories Report SAND97-0047, 1997, p. 22.
20. Greiner, M., Shin, S., Faulkner, R.J. and Wirtz, R.A., "Transport Cask Response to Regulatory Format Thermal Events, Part 1: Rail Package," International J. of Radioactive Material Transport, Vol. 9, No. 3, 1998, pp. 187–192.
21. Greiner, M., Faulkner, R.J. and Jin, Y.Y., "Transport Cask Response to Regulatory Format Thermal Events, Part 2: Truck Cask," International J. of Radioactive Material Transport, Vol. 9, No. 3, 1998, pp. 193–198.